BIOCHEMISTRY
including biophysical chemistry & molecular biology

Article

pubs.acs.org/biochemistry

Fluorescence Anisotropy Uncovers Changes in Protein Packing with Inclusion Growth in a Cellular Model of Polyglutamine Aggregation

Vishal Bhardwaj, Mitradas M. Panicker, and Jayant B. Udgaonkar*

National Centre for Biological Sciences, Tata Institute of Fundamental Research, Bangalore 560065, India

Supporting Information

ABSTRACT: The aggregation of polyglutamine-rich proteins is closely linked with numerous neurodegenerative disorders. In pathological and cellular models, the appearance of protein-rich inclusions in cells acts as a read out of protein aggregation. The precise organization of aggregated protein in these inclusions and their mode of growth are still poorly understood. Here, fluorescence anisotropy-based measurements have been used to probe protein packing across inclusions of varying brightness, formed by an monomeric enhanced green fluorescent protein (mEGFP)-tagged polyglutamine model peptide in cells. High-resolution, confocal-based steady-state anisotropy measurements report a large depolarization, consistent with extensive homo-Förster (fluorescence) resonance energy transfer (FRET) between the sequestered mEGFP-tagged protein molecules. An inverse correlation of fluorescence anisotropy with intensity is seen across inclusions, which becomes emphasized when the observed fluorescence anisotropy values of inclusions are corrected for the fluorescence contribution of the diffusible protein, present within and around smaller inclusions. Homo-FRET becomes enhanced as inclusion size increases. This enhancement is confirmed by two-photon excitation-based time-resolved fluorescence anisotropy decay measurements, which also suggest that the mEGFP-tagged protein molecules are arranged in multiple ways within inclusions. Bright inclusions display faster FRET rates with a larger number of mEGFP moieties participating in homo-FRET than faint inclusions do. These results are consistent with a model in which the protein is more closely packed in the brighter inclusions. In such a possible mechanism, the higher packing density of protein molecules in brighter inclusions would suggest that inclusion growth could involve an intermolecular compaction event within the inclusion, as more monomers and aggregates are recruited into the growing inclusion.

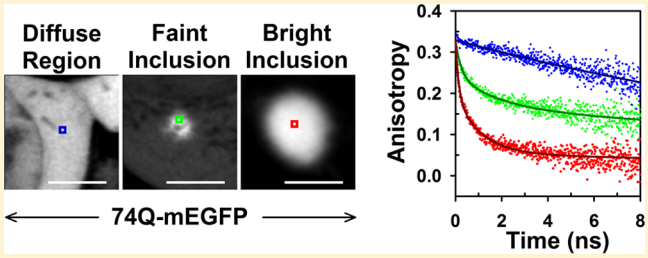

Protein aggregation and inclusion body formation by a set of polyglutamine (poly-Q)-expanded proteins are known to be associated with a number of neurodegenerative disorders.[1,2] Huntingtin is one such poly-Q-expanded, aggregation-prone protein that has been shown to form aggregates *in vitro*, in cells, and in animal models.[3−6] The aggregation propensity of huntingtin protein and the frequency of inclusions observed in patients have been shown to be dependent on the length of the poly-Q segment.[7,8] Huntingtin has been shown to form a wide variety of aggregate-related structures, ranging from large fibrils to smaller aggregates and soluble oligomers *in vitro*.[3,9−12] Under *in vitro* conditions, aggregation has been described as a nucleation-based model, with fibrils and large aggregates as the final end products.[9,13] The aggregation mechanism becomes altered as a function of poly-Q repeat length and of the protein sequence flanking the poly-Q segment.[11,14] In cells, expression of poly-Q-expanded huntingtin (Q_n >35−40) results in the accumulation of the protein in large inclusions.[8] The truncated N-terminal fragment of huntingtin (containing the poly-Q region) shows the remarkably fast appearance of inclusions.[15] The prominent inclusions formed by huntingtin proteins are "insoluble protein deposits" that have been termed IPOD's.[16] The appearance of these inclusions seems to correlate well with cellular survival as opposed to toxicity, thus suggesting a protective role for these inclusions in cells.[17] It appears that diffusible and soluble oligomers, which are formed prior to or escape inclusion body formation, may be responsible for cellular toxicity.[18−20] Understanding the formation and dynamics of aggregate-rich inclusions is important for understanding fully the cellular pathophysiology of poly-Q-associated toxicity and could further suggest means of mitigating the aggregate-associated toxicity.

Several models for describing inclusion growth have been proposed. In one model, an inclusion grows by sequestration of passively diffusible monomeric protein, present in the vicinity of the inclusion.[21] The second mechanism envisages inclusion growth as an aggregation of aggregates. In this scenario, small aggregates formed initially at multiple locations in cells coalesce to form inclusion bodies, at a given site in the cells. Huntingtin inclusions have been suggested to form mainly by the later mechanism, wherein small aggregates are actively transported along microtubules to the site of inclusion body formation.[22] In this regard, huntingtin inclusions resemble a class of inclusions

Received: March 29, 2014
Revised: May 12, 2014
Published: May 12, 2014

   dx.doi.org/10.1021/bi500383h | *Biochemistry* 2014, 53, 3621−3636

known as aggresomes, formed by several other aggregation-prone proteins.[21,23] The mechanism of conversion of smaller aggregates into a large inclusion, as well as the organization of these aggregates within inclusions, is not well understood. A direct probe for looking at interaggregate interaction is required to understand the packing organization of protein molecules in inclusions.

Poly-Q tract-containing aggregation-prone proteins are typically large, varying in size from the 364-residue ataxin-3 to the 3144-residue huntingtin. The observation that for all these proteins, aggregation is driven by the poly-Q tract when it exceeds a certain length has led to the widespread use of the fluorescence of GFP tags attached to just the poly-Q tracts of these proteins to study poly-Q inclusions inside cells.[17,24−27] Although it is possible that the GFP tag may modulate the ability of the poly-Q tract to aggregate in inclusion bodies, just as the protein sequence it replaces could, GFP-tagged poly-Q constructs retain an important property of the original proteins from which the poly-Q tracts are derived: their ability to form inclusions depends on the length of the poly-Q tract.[8] For example, the construct 74Q-GFP, which has the N-terminal fragment of huntingtin exon 1 containing a pathogenic poly-Q length of 74 glutamine residues tagged with GFP (Figure 1A), forms inclusions, while the construct 23Q-GFP, containing the shorter nonpathogenic poly-Q length of 23 glutamine residues, does not form inclusions in cells.[28]

The ability to use GFP-tagged poly-Q tracts to study inclusion body formation has allowed the widespread use of fluorescence or Förster resonance energy transfer (FRET) measurements to report on inclusion body formation. For example, hetero-FRET-based measurements have suggested that huntingtin molecules are organized in the proximity of each other in inclusions.[19,26,27] Hetero-FRET measurements are easier to interpret when the molecules are organized in smaller clusters. In larger clusters, the precise relationship between the cluster size and the extent of FRET observed becomes complex, as FRET can occur in multiple ways, and because the donor- and acceptor-tagged proteins may be present in an unknown stoichiometry in the inclusion. FRET can also occur between identical fluorophores separated by short distances (homo-FRET). Homo-FRET leads to a sharp reduction in the observed fluorescence anisotropy value,[29,30] which is proportional to the extent of FRET and therefore provides a direct measure of the packing density with which GFP-tagged protein molecules are organized. Thus, anisotropy measurements are ideal for looking at large clusters of closely organized molecules and for probing a number of protein aggregates and oligomers.[30−37]

In this study, high-resolution confocal microscopy-based, steady-state fluorescence anisotropy imaging was conducted on inclusions formed by an mEGFP-tagged, poly-Q-containing peptide from the huntingtin protein in mammalian cells. These measurements were complemented with high-resolution two-photon, time-resolved fluorescence anisotropy decay measurements. Steady-state anisotropy measurements showed that the fluorescence anisotropy values in inclusions are much lower than in diffusely expressing (aggregate-free) regions. The extent of the reduction in anisotropy values was found to correlate inversely with the fluorescence intensity of the inclusions and can be attributed to homo-FRET. In the time-resolved anisotropy measurements too, bright inclusions showed a higher degree of homo-FRET than the fainter inclusions. The protein molecules in the larger and brighter inclusions appear to be more closely packed and are arranged in larger clusters, compared to the protein molecules in smaller and relatively fainter inclusions. As the relative amount of aggregated protein is greater in large inclusions, it appears that the packing density of the aggregated protein is considerably higher in the larger inclusions. Inclusion growth appears to be accompanied by an increase in protein packing density.

MATERIALS AND METHODS

Recombinant DNA Constructs. Plasmids encoding truncated huntingtin exon 1 with polyglutamine tracts with lengths of 23 (normal) and 74 (pathogenic) residues were used for protein expression in cells (Figure 1A). Both constructs contained amino acid residues 8−57 of normal human huntingtin protein in the pEGFP C-1 vector.[28] The N-terminal EGFP moiety in both constructs was further converted to monomeric form (mEGFP) by introducing the A206K mutation,[38] using site-directed mutagenesis. mEGFP (pEGFP C-1) was also expressed alone in cells, as an independent control for anisotropy measurements.

Cell Culture and Transfection. HEK-293T (Lenti-X, Clontech) cells were maintained in Dulbecco's modified Eagle's medium (DMEM, high glucose, Gibco) with 10% fetal bovine serum (FBS, Gibco) and grown in 5% CO_2 at 37 °C. Cells were plated and grown overnight on poly-D-lysine (PDL, Sigma)-coated coverslip bottom dishes before being transfected. Transfections were conducted with Fugene 6/HD reagents (Roche), as per the manufacturer's recommended protocols. Approximately 200 to 250 ng of plasmid DNA was used to transfect the cells in each coverslip dish, in a volume of 200−250 μL. Cells were imaged in Dulbecco's phosphate-buffered saline [DPBS (pH 7.4), Gibco] with calcium, magnesium, and glucose, or in HEPES-buffered Hank's Balanced Salt Solution [HBSS (pH 7.4), Gibco].

Steady-State Anisotropy (SSA) Imaging. Steady-state anisotropy imaging was conducted using a LSM 5 LIVE microscope (Zeiss Confocal Systems, Jena), custom designed for measuring steady-state fluorescence emission anisotropy.[39] A high-NA objective (63×, 1.4NA) combined with high zoom settings (pixel size of 100 nm) was used to capture high-resolution images. Emitted fluorescence from samples was split into parallel and perpendicular polarized fluorescence by a polarizing beam splitter. Individual polarized emissions were passed through slits to achieve confocality (slit width of ∼1.19 airy units, z slice thickness of <1 μm). Polarized emissions were further filtered by matched 495−555 nm band-pass filters and were focused onto two linear CCD detectors. Cells were imaged with a low laser power to avoid photobleaching due to imaging. All images acquired were averages of two frames. For all imaging experiments, fluorescein at pH 11 (1 mM NaOH) was used as the G-factor control (explained below), while a recombinant EGFP solution (pH 8, Tris) was imaged as an anisotropy control.

The imaging of a large number of inclusion-containing cells encompassing a wide range of intensity values was conducted under different imaging conditions (Figure 2C). Briefly, the camera gain, scan speed (exposure time), and laser power were adjusted to obtain sufficiently bright images of each inclusion. Images of the fluorescein solution were also acquired under these different imaging conditions. The relative intensity of the fluorescein solution was used as a reference for normalizing across images of different inclusions.

The LSM DUO-SCAN module attached to LSM 5 LIVE was used for conducting photobleaching along with SSA imaging.[39] Here SSA images were acquired with the line-scanning LIVE

module, while precisely patterned photobleaching was achieved by the point-scanning DUO module. For photobleaching of inclusions, a modified fluorescence recovery after photobleaching (FRAP)-like strategy was used in a repeated manner.[40] Briefly, images of inclusion-containing cells were first acquired in the anisotropy imaging mode. This was followed by a short pulse (<2 s) of iterative photobleaching in a region containing the entire inclusion. The photobleached inclusion was imaged again after a gap of 10 s, to avoid any contribution of reversible photobleaching. To achieve a sufficiently reduced intensity (<25% of prebleach intensity) in inclusions, repeated cycles of imaging and photobleaching were conducted.

A modified fluorescence loss in photobleaching (FLIP)-like strategy was employed for reducing the contribution of diffuse monomeric protein from the observed anisotropy of aggregated protein.[40] Briefly, an inclusion-containing cell was imaged in anisotropy mode (as described above). A small region (3−4 μm^2 wide) away from the inclusion was iteratively photobleached for 10−20 s. The same inclusion-containing cell was imaged again after 60 s, allowing bleached molecules present outside the inclusion to become equilibrated with the diffusible protein present within the inclusion.

Generation of Whole Frame SSA Images. All image analysis was conducted with FIJI/ImageJ.[41] Parallel and perpendicular polarization images were aligned with the help of the "Descriptor Based Registration" plugin.[42] Images of subresolution (~200 nm wide) fluorescent beads acquired under similar imaging conditions were used as reference images for alignment. Aligned images were buffer corrected, followed by nearest neighbor averaging (mean filter with a one-pixel radius). To remove instrument bias between the two detectors at a pixel by pixel level, a *G* factor correction was applied to the images. Fluorescein is a small fluorescent molecule that tumbles very fast with a rotational correlational time of ~120 ps, resulting in a nearly complete depolarized emission during the imaging time window (pixel dwell time of >20 μs). The *G* factor image refers to a correction image obtained by dividing the parallel intensity image with the perpendicular intensity image, of a dilute solution of fluorescein.

$$G = \frac{I_{\parallel}}{I_{\perp}}(\text{fluorescein}) \tag{1}$$

Parallel and perpendicular intensity images of a fluorescein solution were also buffer corrected and nearest neighbor filtered, as in the case of the cell images, before the *G* factor image was created. A precise *G* factor image was made by averaging a stack of five to seven individual *G* factor images.

This *G* factor correction was applied to all perpendicular polarization images of cells and control fluorophore (GFP) solutions. Whole frame SSA images (r) were thus calculated as follows:

$$r = \frac{I_{\parallel} - GI_{\perp}}{I_{\parallel} + 2GI_{\perp}} \tag{2}$$

and total intensity (I_{Total}) images were calculated as

$$I_{\text{Total}} = I_{\parallel} + 2GI_{\perp} \tag{3}$$

Total intensity images were thresholded to highlight the regions of interest, i.e., whole cells when protein expression was diffuse and inclusions for aggregate-containing cells. The same threshold binary maps were applied to the corresponding anisotropy images. In the photobleaching assay, each round of photobleaching reduces the intensity values of some regions around the inclusion to below the set threshold value (0.1 times the prebleach peak intensity pixel value in Figure 3A). The intensity and anisotropy information in these regions thus is filtered from the image, which leads to the impression that the inclusion has become smaller after photobleaching. Anisotropy images were pseudocolored to an appropriate scale (Royal LUT, FIJI). On the basis of the anisotropy images of the EGFP solution, all the analysis of cells was limited to a region at the center of the image frame (central 350 pixel × 450 pixel region out of the 512 pixel × 512 pixel frame) where the anisotropy variation remained minimal and constant across measurements. The mean SSA of the EGFP solution measured at the center of the frame was 0.252 ± 0.005. Fluorescein solution images acquired under similar imaging conditions were used as reference images for correcting the total intensity images of cells against nonuniform illumination across the image frame.

Analysis of the Whole Frame SSA Images. *Diffuse Regions.* The average SSA of nonaggregated 74Q-mEGFP protein, with or without small aggregates present elsewhere in expressing cells, was compared to the average anisotropies of mEGFP and 23Q-mEGFP proteins expressed in cells, as follows (Figure 1C). Anisotropy values from 50 small regions of 5 pixel × 5 pixel widths (0.25 μm^2 wide) were recorded from each cell, and a distribution of anisotropy values was generated for each construct. The individual distributions were fit to a Gaussian function, providing an average value of anisotropy (with the standard deviation) for each construct.

Inclusions. The average steady-state intensity and anisotropy values of aggregated 74Q-mEGFP protein were compared for a large number of inclusion-containing cells as follows (Figure 2C). The average intensity and anisotropy values from a small, 3 pixel × 3 pixel (0.09 μm^2) wide region at the center of each inclusion were recorded for a number of inclusion-containing cells. The width of the chosen region was kept deliberately small, to compare even the smallest of inclusions, with a size comparable to the point spread function (PSF) of the objective.

Intensity−Anisotropy Distribution of Inclusions and Two-Component Model Fitting. For each inclusion-containing cell, a rectangular region containing the aggregated protein was selected from the total intensity and its respective anisotropy image. The chosen regions were sufficiently wide to span a small margin of diffuse, nonaggregated protein present around the inclusions. For each region, intensity and anisotropy values from all pixels were recorded. The intensity values were further divided into 8−15 small bins of equal intensity intervals. The intensity and anisotropy values of all pixels contained in the individual intensity bins were averaged, to obtain single mean values of intensity and anisotropy, with their respective standard deviations. The mean values of anisotropy were plotted against their intensity values, for all intensity bins. To reduce noise, low-intensity regions were omitted (if required). The intensity−anisotropy distributions of faint and small inclusions were analyzed by the two-component model (see below).

The two-component model presumes that the inclusion-containing region of a cell is composed of aggregated protein (A) and diffusible protein (D). For a mixture of fluorophores, the total intensity of the mixture is given by the linear sum of the intensities of the individual components. The total anisotropy value observed for such a mixture is given by the weighted sum of the individual anisotropies of the two components, weighted by their fractional intensity contributions toward the observed total intensity. Thus, the observed steady-state intensity (I_{Total}) and

dx.doi.org/10.1021/bi500383h | *Biochemistry* 2014, 53, 3621−3636

anisotropy (r_{Total}) value from a given part of an inclusion can be represented as

$$I_{Total} = I_D + I_A \quad (4)$$

and

$$r_{Total} = \frac{I_D r_D + I_A r_A}{I_{Total}} \quad (5)$$

where I_D and I_A are the apparent intensities of the diffusible and aggregated protein present in any given part of the inclusion, respectively, and r_D and r_A are the corresponding values of the fluorescence anisotropies.

Upon rearrangement of eqs 4 and 5, the observed anisotropy in a given part of an inclusion is described by

$$r_{Total} = r_A + \frac{I_D(r_D - r_A)}{I_{Total}} \quad (6)$$

Equation 6 represents a linear sum of two terms; hence, for a given fixed value of r_{Total}, a solution with highest values of r_D and I_D used would yield a lowest value of r_A. Thus, the predicted value of aggregate anisotropy (r_A), with the assumptions used (see Results), represents the lowest possible value, capable of explaining the observed distribution. The actual value of aggregate anisotropy could be anywhere within the interval of the observed value (upper bound) and the predicted value (lower bound).

Time-Resolved Anisotropy (TRA) Decay Measurements. Time-resolved anisotropy measurements from cells were taken using a LSM 510 Meta confocal microscope (Zeiss Confocal Systems) with a 63× (NA 1.4) objective.[43] A Mai-Tai Ti-Sapphire (Spectra physics) mode-locked laser tuned at 920 nm was used to achieve two-photon excitation of mEGFP. To achieve a single G factor across measurements, the excitation beam was parked at the center of the frame, and all measurements were made at this point. The emitted photons were directed to the nondescanned port by a 680 nm reflector (Zeiss) and were further filtered by an EGFP emission filter. The emitted photons were then separated into parallel and perpendicular polarized components by a polarization beam splitter and were collected simultaneously by two R3809U MCP photomultiplier tubes (Hamamatsu). TCSPC traces were acquired with a SPC-830 (Becker and Hickl) card working in "Stop-Start" mode. All traces were acquired at an 80 MHz excitation repetition rate with an acquisition time resolution of 12.2 ps per channel. To satisfy TCSPC criteria, and to avoid any pulse pile-up effect, emitted photons were acquired at a count rate of <0.2 MHz. Colloidal gold particles dried on a coverslip were used to measure the instrument response function (IRF). A dilute solution of fluorescein at pH 11 was used for measuring the G factor, and an EGFP solution was used as an anisotropy control. The instrumentation easily allowed the resolution of the fast TRA decay of fluorescein [100−140 ps decay constant (data not shown)]. The measured TRA decay constants of fluorescein and EGFP were found not to significantly vary across experiments.

Analysis of TRA Decay Traces. Individually polarized fluorescence traces (parallel and perpendicular intensity decays) for all samples were first aligned with each other along their rising edges and were background corrected. The channel with peak counts in similarly aligned IRF traces was used as the start channel for all decays (t_0). The G factor value was calculated by matching the tails of the two polarized traces of fluorescein solution, at long time points (2 ns onward). Time-dependent anisotropy, $r(t)$, was calculated for each sample using the following equation:

$$r(t) = \frac{I_{||}(t) - GI_{\perp}(t)}{I_{||}(t) + 2GI_{\perp}(t)} \quad (7)$$

Similarly, a fluorescence lifetime (total intensity) trace, $I(t)$, was generated as

$$I(t) = I_{||}(t) + 2GI_{\perp}(t) \quad (8)$$

The observed TRA traces showed a minor distortion in the form of an apparent fast decay at the start of all traces, which presumably represents an effect of the IRF. The full width at half-maximum (fwhm) of the IRFs for both detectors was <50 ps. Hence, the calculated TRA traces were directly comparable after the initial 60−100 ps. For a simple comparison, the observed TRA traces were fit directly to nonlinear, least-squares, sum of exponential decay models, based on the following equation:

$$r(t) = r_0 \sum_{i=1}^{n} A_i e^{-t/\tau_i} \quad (9)$$

and

$$\sum_{i=1}^{n} A_i = 1 \quad (10)$$

where n = 1, 2, and 3 for one-, two-, and three-exponential decays, respectively.

Here r_0 refers to the apparent initial anisotropy, observed at time t_0. τ_i and A_i represent the individual apparent anisotropy decay time and the corresponding amplitude, respectively.

As mentioned above, because of initial IRF distortion, the initial parts of all traces (60−120 ps) were not fitted. The intensity values in the total intensity traces were normalized to the intensity in the first channel of the given trace, from where the TRA traces were to be fitted. These normalized intensity traces were then used as the weights for fitting the corresponding anisotropy decay traces. TRA traces from mEGFP-expressing cells were fitted to a single-exponential decay model, and a range of apparent r_0 values were recovered by back extrapolating fits to time t_0. The r_0 values remained between 0.32 and 0.345 for mEGFP- and diffuse 74Q-mEGFP-expressing cells. These values were used as a reference for describing TRA traces from 74Q-mEGFP inclusion-containing cells. In the three-exponential fitting for TRA traces of inclusions, the longest correlation time was constrained to be >40 ns. This number is not reliable as the amplitude of the rotational component was very low. The actual slow rotational correlational time is likely to be much higher (>100 ns). All fitting analyses were conducted using SigmaPlot (Systat).

RESULTS

In this study, intracellular inclusions formed by an mEGFP-tagged poly-Q-expanded peptide were examined by fluorescence anisotropy-based measurements. For observing rapid and efficient inclusion body formation in cells, an N-terminal fragment of huntingtin exon 1 containing a pathogenic poly-Q length of 74 glutamine residues (74Q) was expressed in HEK-293T cells (Figure 1A).[28] A similar peptide with a shorter nonpathogenic poly-Q length of 23 glutamine residues (23Q) was used as a nonaggregating control protein. HEK-293T cells were used for transient expression because of the relative ease of transient transfections and high protein expression levels. HEK-

dx.doi.org/10.1021/bi500383h | Biochemistry 2014, 53, 3621−3636

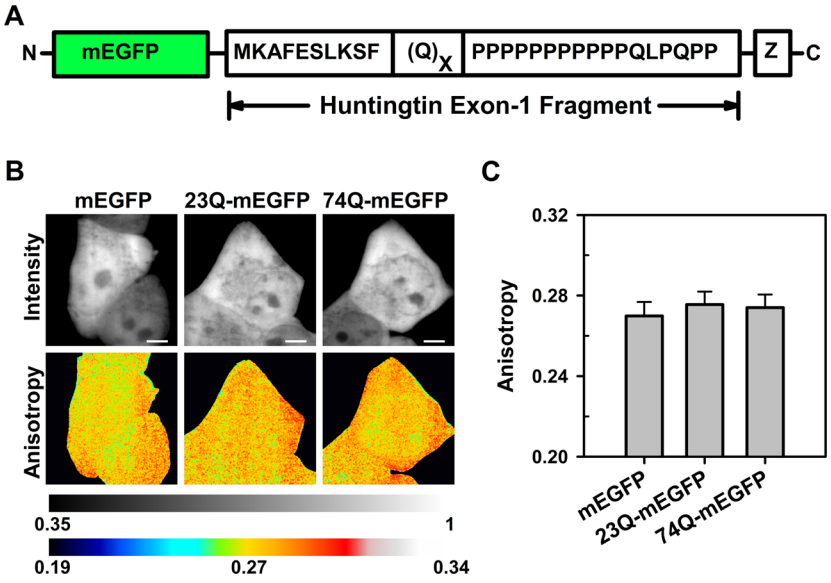

Figure 1. Steady-state anisotropy imaging of inclusion-free poly-Q mEGFP-expressing cells. (A) Schematic description of the polyglutamine constructs expressed in HEK-293T cells. The truncated human huntingtin exon 1 peptide was tagged with mEGFP. Two different lengths of polyglutamine tracts were used for transient expression of control ($X = 23$) and aggregation-prone ($X = 74$) huntingtin peptides. The proline-rich sequence of huntingtin exon 1 is followed by a few amino acid residues contributed by the pEGFP vector (Z). (B) Confocal steady-state intensity (gray scale) and anisotropy (pseudocolored) images of HEK-293T cells expressing mEGFP, 23Q-mEGFP, and 74Q-mEGFP, imaged 24 h post-transfection. The 74Q-mEGFP-expressing cell shown is visibly devoid of inclusions. (C) Mean steady-state anisotropy values, with standard deviations as error bars, obtained from 60 cells in each of the three categories of cells shown in panel B. For 74Q-mEGFP, measurements from visibly diffuse (inclusion-free) regions of cells were included. The scale bar is 5 μm.

293 cells have been used previously in various studies of inclusion and oligomer formation, as well as for the purification of aggregates and cellular interacting partners of aggregating proteins.[8,20,44−46] mEGFP was also expressed separately in cells, as a control for measuring the fluorescence anisotropy of the fluorophore alone.

The transient expression of 74Q-mEGFP resulted in the appearance of inclusions in some cells, visualized 24 h post-transfection. These inclusions were formed in the cytoplasm, in the vicinity of the nucleus. The inclusion-containing cells were clearly distinguishable from the rest of the 74Q-mEGFP-expressing cells that did not show any visible aggregates at the time of the imaging. Inclusions ranged from small and faint (size of <2 μm) with a punctate appearance to large and bright (size of >4 μm) with a bloblike morphology. Inclusions were found to grow in size and intensity over a 5−10 h period from the time they were first observed [approximately 24 h post-transfection (Figure S1 of the Supporting Information)] and were found to start to grow in different cells at different times. Hence, inclusions of varying brightness and size inside different cells at the same point in time can be taken to be inclusions at different stages in their growth. In contrast, 23Q-mEGFP-expressing cells did not show any visible aggregates and showed only diffusely distributed protein. Notably, the distribution of 23Q-mEGFP in over-expressing cells was virtually indistinguishable from that in the inclusion-free 74Q-mEGFP-expressing cells (Figure 1B).

Fluorescence anisotropy measurements of cells expressing different mEGFP-tagged proteins were conducted using high-resolution objectives (~63×, 1.4 NA), so that the smaller size inclusions (diameter of <1 μm) could clearly be differentiated from the aggregate-free regions. Fluorescence anisotropy measurements taken with high-NA objectives show significant depolarization and compression of the fluorescence anisotropy scale because of the mixing of individual polarized light components.[47] Steady-state anisotropy (SSA) imaging was conducted using a line-scanning confocal (slit-based) microscope, which allowed fast imaging with a sufficiently large anisotropy scale (Materials and Methods). Time-resolved anisotropy (TRA) measurements were taken using two-photon excitation of the mEGFP moieties. Two-photon excitation expands the scale of observed anisotropy; hence, some of the loss in the dynamic range of fluorescence anisotropy measurements due to the use of a high-NA objective is partially compensated for.[48] It is important to note that while the use of a high-NA objective compresses the dynamic range, the determination of decay rate constants is unaffected.[33]

Steady-State Fluorescence Anisotropy Profiles of Cells Expressing mEGFP-Tagged Poly-Q-Containing Peptides. Figure 1B shows representative whole cell SSA images of cells expressing the three mEGFP-tagged proteins, with diffuse expression of the individual proteins. The fluorescence anisotropy of protein molecules in different regions of cells expressing any of the three proteins appeared to be similar. The average value of fluorescence anisotropy observed in regions of cells showing diffuse (inclusion-free) expression of 74Q-mEGFP was compared with that in the cells expressing 23Q-mEGFP or mEGFP-alone (Materials and Methods and Figure 1C). As expected, the SSA values measured from mEGFP-alone-expressing cells were fairly high ($r_{average} \sim 0.27$). Similar anisotropy values were observed in cells expressing 23Q-mEGFP and diffuse 74Q-mEGFP. The similarity in the fluorescence anisotropy values suggests that the observed anisotropy values are dominated by the large (240 residues) mEGFP moiety; linkage of either poly-Q-containing peptide to the mEGFP moiety does not change the latter's anisotropy.

A similar analysis was conducted with cells containing 74Q-mEGFP inclusions (Materials and Methods). Figure 2A shows representative steady-state intensity and anisotropy images of

dx.doi.org/10.1021/bi500383h | *Biochemistry* 2014, 53, 3621−3636

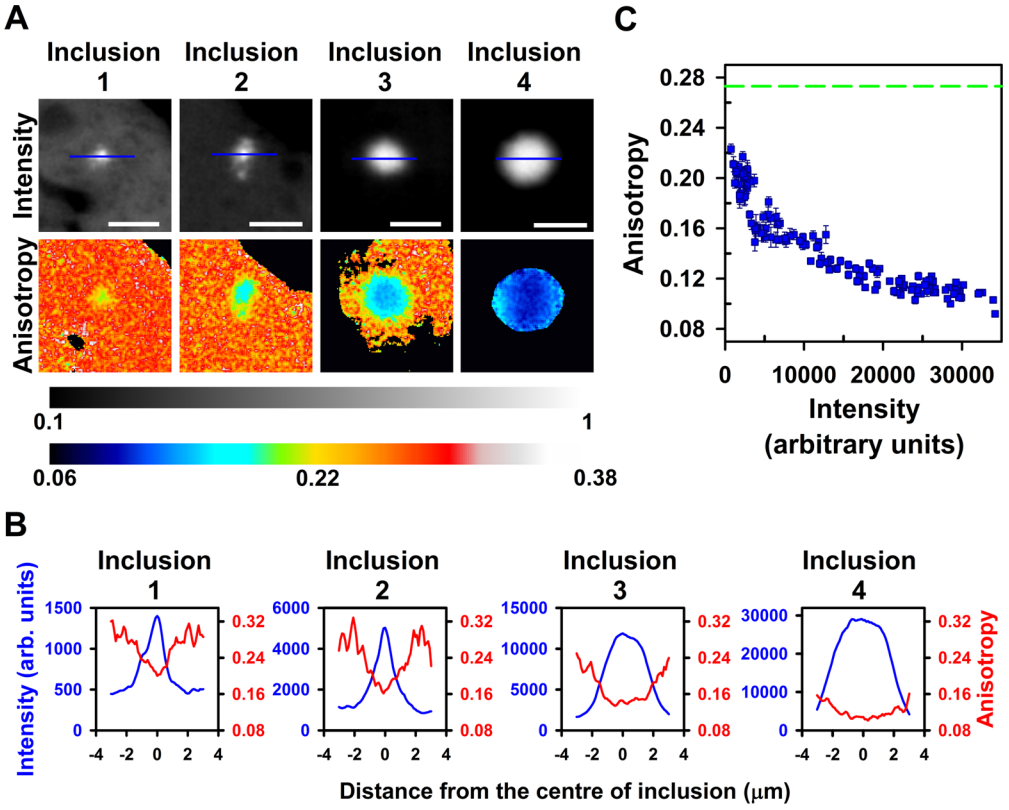

Figure 2. Highly depolarized anisotropy in aggregate-rich, mEGFP-tagged poly-Q inclusions. (A) Steady-state intensity (gray scale) and anisotropy (pseudocolored) images of representative cells containing polyglutamine inclusions. The inclusion-containing cells are arranged in increasing order of peak intensity, from inclusion 1 to inclusion 4. The intensity images have been further rescaled by normalizing the intensity values of every pixel in the image with the peak intensity value observed in the inclusion. Intensity and anisotropy images shown have also been thresholded to filter low-intensity regions, with all intensity values being <10% of the peak value being removed. (B) Plots with absolute intensity values for these inclusions, which show intensity (blue) and anisotropy (red) profiles of the inclusions, determined across the lines drawn through the center of the inclusions, as shown in panel A. (C) Apparent correlation of average steady-state anisotropy, *r*, with intensity, *I*, observed in 135 inclusions (blue squares). Each point in the plot represents the average intensity and anisotropy values measured from a small region at the center of each inclusion (with standard deviations as the error bars). The dashed green line represents the average value of steady-state anisotropy measured from aggregate-free regions of 30 poly-Q74-expressing cells, highlighting the extent of depolarization seen in inclusions. The scale bar is 5 μm.

different inclusion-containing cells, arranged in an increasing order of intensity. All inclusions that showed high fluorescence intensity displayed fluorescence anisotropy values that were significantly lower than values in nearby diffuse regions. The fluorescence intensity appears to be highest, and the fluorescence anisotropy appears to be lowest at approximately the center of each inclusion (Figure 2B). The bright inclusions displayed SSA values much lower than the relatively faint inclusions; the center of inclusion 4 in Figure 2A displayed the highest intensity value and the lowest fluorescence anisotropy value among the four inclusions. The fluorescence anisotropy is seen to increase from inclusion 4 to inclusion 1, correlating inversely with size and intensity.

Figure 2C illustrates this inverse correlation quantitatively for a large number of inclusions, spanning a wide intensity range (see Materials and Methods). The SSA values observed at the centers of inclusions were significantly lower than the average SSA value displayed by cells devoid of large inclusions (Figure 2C). The SSA values observed for the bright inclusions were one-half to nearly one-third of those observed for aggregate-free diffuse regions, signifying the extensive depolarization observed in inclusions. It should be noted that the spread in SSA values at any given intensity value is small compared to the range of SSA values seen across inclusions.

Homo-FRET Is Responsible for the Observed Low Steady-State Anisotropy Values in Inclusions. The possibility that the low fluorescence anisotropy observed in the 74Q-mEGFP inclusions is indeed due to homo-FRET was tested by a photobleaching-induced anisotropy recovery assay.[30,33,36,49] Photobleaching brings about a reduction in the density of active fluorophores, thus effectively decreasing the number of fluorophore pairs involved in FRET, which leads to an increase in fluorescence anisotropy. Figure 3 shows the change in the SSA of an inclusion upon photobleaching. Photobleaching across the entire inclusion was conducted in intermittent pulses alternated with imaging cycles (Figure 3A). It is seen that the fluorescence anisotropy of the entire inclusion increases with a concomitant photobleaching-induced reduction in intensity. Figure 3B shows how the SSA value measured at the center of the inclusion, increases with a decrease in intensity at the center of the inclusion. The data in Figure 3 validate the interpretation that the cause of depolarization is strong homo-FRET between the closely packed mEGFP moieties in the inclusions.

Estimating the Actual SSA Values of Aggregated Protein within an Inclusion. Inclusion body formation by 74Q-mEGFP involves a time-dependent sequestration of diffusing protein molecules into the inclusions (Figure S1 of the Supporting Information). At an early time point of the observation, when an inclusion body is small and faint (Figure 4),

dx.doi.org/10.1021/bi500383h | *Biochemistry* 2014, 53, 3621−3636

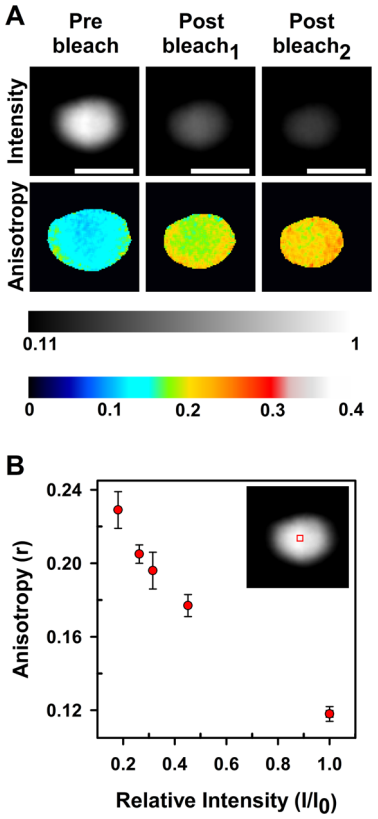

Figure 3. Steady-state anisotropy of an inclusion increases upon photobleaching. (A) Steady-state intensity (gray scale) and anisotropy images (pseudocolored) of an inclusion before (prebleach) and after two successive rounds of photobleaching (postbleach$_1$ and postbleach$_2$). Intensity images have been normalized to the peak intensity pixel value of the prebleach image frame. Intensity and anisotropy images have been thresholded to filter low-intensity regions, as in Figure 2A. (B) Change in anisotropy (r) with a decrease in intensity (I) for the inclusion, upon four successive rounds of photobleaching. Each point (red circles) in the plot represents the mean intensity and anisotropy value measured at a given time point, from a small region highlighted by a red square in the intensity image, shown in the inset. Intensity values (I) after each round of photobleaching were normalized to the prebleach intensity value (I_0). The scale bar is 5 μm.

the amount of diffusible protein (D) would dominate over that of the aggregated protein (A). As the inclusion body growth progresses, the relative amount of diffusing protein within and around an inclusion decreases; however, at all times during the process, diffusible protein is present in the vicinity of the inclusion. Thus, the fluorescence intensity and anisotropy values measured from inclusions include contributions from both these pools. A reduced value of fluorescence anisotropy in bright inclusions could just be because they contain less diffusible protein, while the actual value of the fluorescence anisotropy of the aggregated protein is similar to that of the aggregated protein in a faint inclusion. If this was the case, then it would imply that no structural change occurs in the aggregates along with inclusion growth. On the other hand, if the SSA value for the aggregated protein in the bright inclusions is actually lower than the same in faint inclusions, it would suggest that the organization of protein molecules within the aggregate changes upon inclusion growth. To differentiate between these two scenarios, it is important to know the actual value of the fluorescence anisotropy for the aggregated protein in an inclusion. The impact of the presence of diffusible protein within and around the aggregated material on the observed values of anisotropy for any given inclusion can be estimated by a simple two-component model (see eq 6 in Materials and Methods).

The two-component model is based on several assumptions. (1) It assumes that the measurements of intensity (I_{Total}) and anisotropy (r_{Total}) in each image pixel contain the contributions of the aggregate intensity (I_A) and anisotropy (r_A) as well as of the diffusible protein intensity (I_D) and anisotropy (r_D) (see eqs 4 and 5 of Materials and Methods). (2) It is assumed that the value of r_A is constant throughout the inclusion, implying that if there is any heterogeneity in r_A values within an inclusion it can still be represented by an average r_A value. This assumption appears to be reasonable given the spatial resolution of our measurements is such that any spatial heterogeneity in r_A values within an inclusion is not directly measurable; hence, the simplest possible assumption is made regarding the structure (and hence r_A) of the aggregate within an inclusion. (3) It assumes that the value of r_D is the same throughout the inclusion and is the same as that of the diffusible protein present just outside the periphery of the inclusion because it is this protein that diffuses into the inclusion. Hence, the value of r_D was fixed at the constant value obtained for diffuse 74Q-mEGFP (Figure 1C). (4) It is also assumed that I_D is uniform throughout the inclusion and in the immediate vicinity of the inclusion, which implies that the diffusible protein has equilibrated throughout and just outside the inclusion. It should be noted that this assumption would not be valid if the packing density varies drastically throughout the inclusion, which might lead to a diffusion gradient within the inclusion, or if binding of the diffusible protein to the aggregate occurs faster than the fluorescence lifetime (nanoseconds), which is unlikely.

The two-component model was first tested on faint small inclusions. Figure 4A shows that correlation of fluorescence anisotropy with intensity within a faint inclusion. It should be noted that faint inclusions are small (diameter of <2 μm), and because the z slice thickness of the confocal microscope is ~1 μm, the measurement would include contribution from diffusible protein present immediately below and above the inclusion. It is seen that the data are described well by eq 6 based on the two-component model. Importantly, this agreement of the data with the minimalistic two-component model suggests that the assumptions on which the model is based are reasonable at least for faint inclusions. The two-component model was found to also describe well the SSA−intensity correlation of inclusions of intermediate brightness (see below).

The fit to eq 6 predicts the value of I_D for diffusible protein present within and immediately above and below the inclusion and also predicts the value of r_A. It should be noted that the value predicted for r_A is a lower bound to its true value because of the assumption that the value of I_D is uniformly high throughout the inclusion, as high as that present in the immediate vicinity of the inclusion. Figure 4B shows curves simulated on the basis of the two-component model, in which a given amount of diffusible protein is mixed with an increasing amount of aggregated protein. As expected, the fluorescence anisotropy of the simulated curve approaches the actual value of aggregate anisotropy, when the contribution of diffusible protein is lowest.

The Aggregate Anisotropy Value Predicted by the Two-Component Model Represents a Lower Bound on the Actual Value of Aggregate Anisotropy. Figure 5 shows a faint inclusion-containing cell (prebleach case), with the inclusion-containing region highlighted by a blue square. The

dx.doi.org/10.1021/bi500383h | Biochemistry 2014, 53, 3621−3636

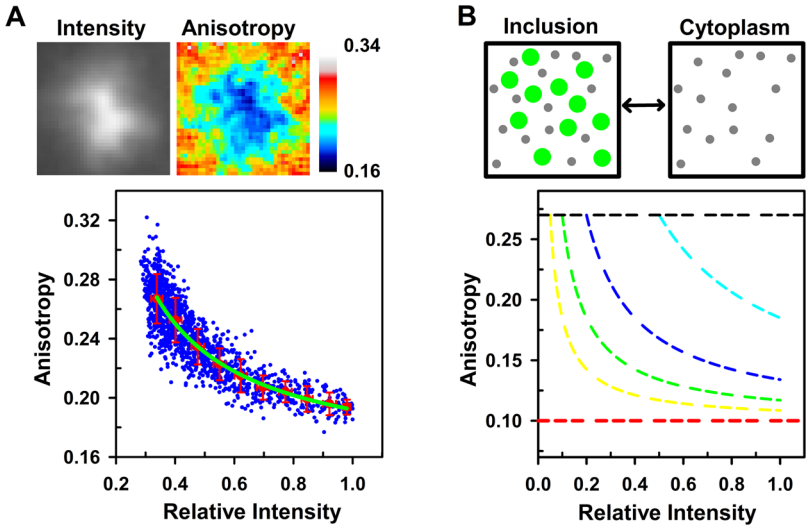

Figure 4. Contribution of diffusible protein to the observed fluorescence anisotropy value of an aggregate-rich inclusion. (A) Steady-state intensity and anisotropy images (pseudocolored) of an inclusion-containing region of a cell (3.8 μm × 3.8 μm). The plot shows the raw distribution of intensity and anisotropy values obtained from all pixels within the region (blue circles). The raw distribution was binned into narrow intensity bins, and their average intensity and anisotropy values are shown as red circles. The green line through the binned data points is a fit of the data to eq 6. (B) Schematic that describes the equilibration of diffusible protein present outside and within the inclusion. Because of simple diffusion, the concentration of diffusible protein present within an inclusion cannot exceed that in the bulk cytoplasmic pool. The plot shows simulated values of anisotropy, obtained by mixing a fixed amount of diffusible protein with an increasing concentration of aggregated protein, in a defined volume. The black and red lines indicate the anisotropy values of the diffuse and aggregated proteins used for simulation. The amount of diffusible protein was varied from 5% (yellow) to 10% (green) to 20% (blue) to 50% (cyan) (represented as the percent fraction occupied by the diffusible pool, at the highest-intensity value).

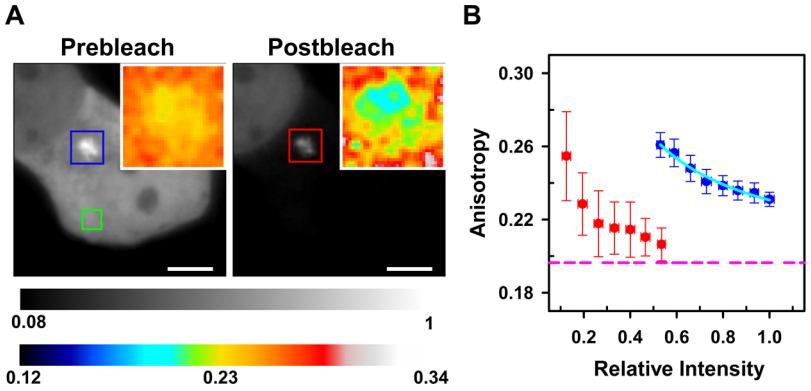

Figure 5. Anisotropy value of aggregated protein obtained from the two-component model-based analysis represents a lower limit to the actual value. (A) Steady-state intensity images of an inclusion-containing cell, before and after the fluorescence of the diffusible pool in the cell had been reduced by continuous photobleaching of a small region, denoted by the green square, outside of the inclusion. The insets in both images depict magnified steady-state anisotropy images of the aggregate-containing region of the cell (blue and red square), before and after diffusible protein outside the inclusion had been photobleached. The anisotropy images have been smoothed by a 1 pixel radius to improve the visual contrast. (B) Binned pixel-wise intensity–anisotropy distributions of the inclusion-containing region before (blue squares) and after (red squares) diffusible protein outside the inclusion had been photobleached. The cyan line represents the fit to eq 6. The dashed pink line at $r = 0.196$ denotes the value of aggregate anisotropy (r_A) for the inclusion obtained from the fit. The intensity values for both distributions have been normalized to the mean intensity value of the brightest bin before the commencement of photobleaching. The scale bar is 5 μm.

pixel-wise distribution of this region fits well to eq 6 of the two-component model (Figure 5B). In the fit, the value of r_D was fixed to the average SSA value observed in diffusely expressing regions of the inclusion-free cells (Figure 1C). The value of r_A was predicted to be 0.196 (Figure 5B), and on the basis of the assumptions of the model, this value represents the lowest possible value of aggregate anisotropy that is capable of explaining the data. It should be noted that when the value used for r_D was varied over a small range, the value obtained for r_A was not affected significantly. It was important to further validate the two-component model for inclusions of faint and intermediate brightness by determining whether the value predicted for r_A by use of the model does indeed match the actual anisotropy value of the aggregated protein within the inclusion.

A photobleaching-based perturbation[40] methodology was used for this purpose (Materials and Methods). A small region in a faint inclusion-containing cell, localized away from the inclusion, was repeatedly photobleached (Figure 5A), to reduce the fluorescence contribution of the diffusible protein present in the cell. The postbleach steady-state intensity image in Figure 5A, taken after the bleached diffusible protein had equilibrated throughout the cell, shows that a major fraction of the diffusible protein pool was photobleached, as indicated by the loss of

dx.doi.org/10.1021/bi500383h | *Biochemistry* 2014, 53, 3621−3636

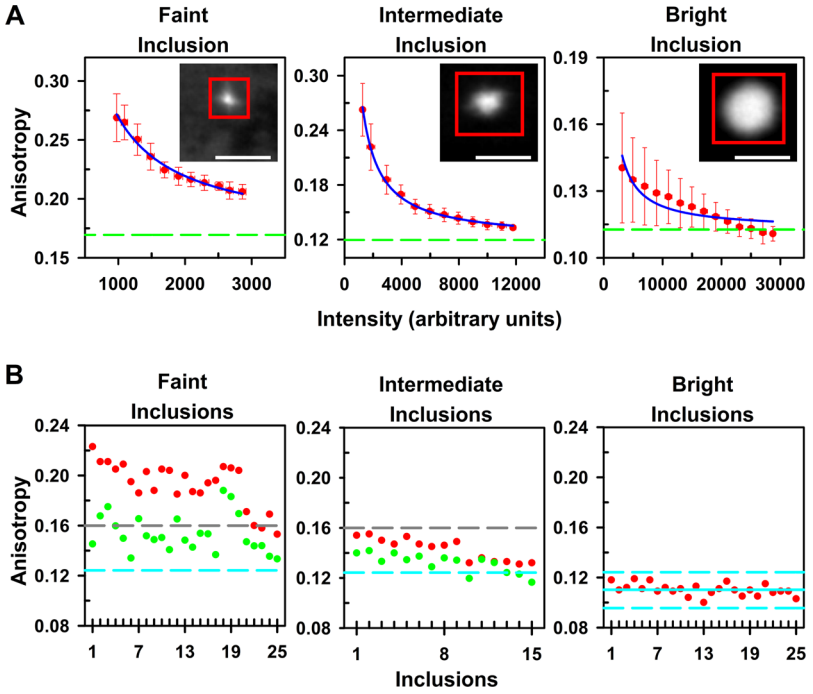

Figure 6. Spread in the steady-state fluorescence anisotropy values in faint, intermediate, and bright inclusions. (A) Representative pixel-wise distributions for faint, intermediate, and bright inclusion-containing cells (insets). The red squares in the intensity images demarcate the inclusion-containing regions. The plots show the binned pixel-wise intensity−anisotropy distributions for the individual inclusions. The intensity−anisotropy distributions of all three inclusions were analyzed using the two-component model, and the blue lines represent the fits obtained. The dashed green line designates the value of r_A, the predicted value of aggregate anisotropy for the individual inclusion in each plot. (B) Anisotropy values observed at the center of inclusions (red circles) and predicted fluorescence anisotropy (r_A) values (green circles) for aggregated protein across multiple inclusions. The left panel shows the data for 25 faint inclusions, which have intensity values of <6000. The middle panel shows the same for 15 intermediate inclusions, which have intensity values between 8000 and 19000. The right panel shows the anisotropy values for 25 bright inclusions, which have intensity values of >25000. The solid cyan line represents the mean anisotropy value obtained from the bright inclusions, and the dashed cyan reference lines demarcate the window of 3 times the standard deviation on either side of the mean anisotropy value. The dashed cyan reference line representing the mean + 3 standard deviations is also shown in the middle and left plot, only to facilitate comparison. A second dashed gray reference line at $r = 0.16$ in the left and middle plots has been drawn by inspection, to further assist in comparison. The intensity images have been rescaled to highlight the peak intensity of the individual inclusions. The scale bar is 5 μm.

intensity around the inclusion. The intensity in the inclusion-containing region was also found to decrease, signifying a loss of diffusible protein present within and around the inclusion. Figure 5B shows the binned pixel-wise distributions of intensity and anisotropy values for the inclusion-containing region, before and after the photobleaching. The observed fluorescence anisotropy value in the postbleach inclusion-containing region is clearly lower than that in the prebleach case. The loss of both fluorescence intensity and anisotropy in the inclusion, after the photobleaching event, occurs because the diffusible protein detected originally with the inclusion has now been replaced by the photobleached diffusible protein from the cytoplasm. The observed loss of intensity and anisotropy cannot be attributed to direct photobleaching of the inclusion or a significant aggregation of bleached monomers into the inclusion (which is very unlikely to have happened within 1−2 min, the duration of the experiment), as in either of these cases, the SSA of the inclusion would have increased post-photobleaching (Figure 3). It should be noted that the SSA of the inclusion-containing region decreases after photobleaching and is only slightly higher than the predicted (lower bound) value of SSA for the aggregated protein, indicating the reliability of the two-component model.

Large and Bright Inclusions Have Significantly Lower Steady-State Anisotropy Values, Compared to Those of Faint Inclusions. Figure 6A shows how well the two-component model describes the pixel-wise intensity−anisotropy distributions of inclusions, of varying brightness. It is seen that the intensity−anisotropy correlation for an inclusion of intermediate brightness is also described well by the model. The observed and predicted values for the intermediate inclusion are found to be lower than those for the faint inclusion but are higher than the observed value for the bright inclusion.

Figure 6A also shows that the two-component model does not adequately describe the intensity−anisotropy correlation of a bright inclusion, whose observed SSA values are well-separated from those of the faint inclusion. For the bright inclusion, the observed value of anisotropy at the brightest region of the inclusion was found to be lower than the value of anisotropy for the aggregated protein predicted by the two-component model. It appears that the assumptions of the two-component model are not valid for the large and bright inclusions. In particular, the assumption that the concentration of the diffusible protein within such an inclusion is uniform throughout the inclusion and the same as that at its periphery is unlikely to be valid because of the tight packing within the large inclusion as suggested by its low observed anisotropy values. It is more likely that a concentration gradient of diffusible protein exists within the inclusion. Second, the application of the two-component model depends on the proper measurement of intensity. The intensity value observed at any point in an image represents a three-dimensional convolution of the point spread function (PSF) of the microscope with the amount of fluorophore. Because of poor z

dx.doi.org/10.1021/bi500383h | *Biochemistry* 2014, 53, 3621−3636

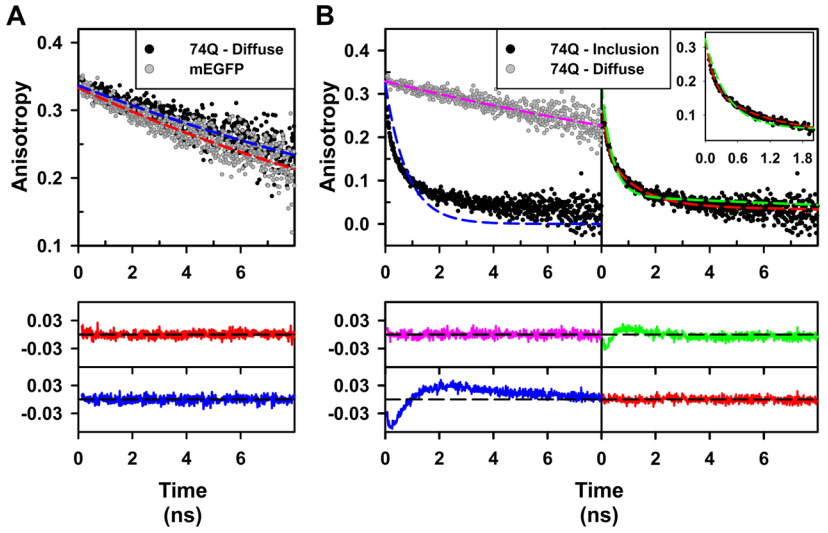

Figure 7. Time-resolved anisotropy decay traces from a 74Q-mEGFP inclusion reveal the presence of multiple decay components. (A) Representative time-resolved fluorescence anisotropy decays from diffuse regions of cells expressing mEGFP (gray circles) and 74Q-mEGFP (black circles). The dashed red and blue lines represent nonlinear, least-squares single-exponential fits for mEGFP and 74Q-mEGFP traces, respectively, with the residuals shown below. (B) Time-resolved anisotropy decay trace recorded from the center of a bright inclusion (black circles), in two adjacent subpanels. A representative decay trace from a 74Q-mEGFP-expressing cell displaying only diffuse expression (gray circles) is shown in the left subpanel, as a reference for the initial anisotropy. The dashed pink and blue lines in the left subpanel represent nonlinear, least-squares single-exponential fits for the protein in the diffuse region and in the inclusion, respectively. The dashed green and red lines in the right subpanel are the two- and three-exponential fits for the inclusion, respectively. The inset in the right subpanel shows the two- and three-exponential fits in the first 2 ns of the TRA decay. The residuals for all the fits are shown below the decay traces.

resolution and imperfect confocality (slits), intensity measurements within a large inclusion could be skewed because of the contribution of aggregated protein present above and below the z slice. For smaller inclusions of faint and intermediate brightness, whose dimensions are comparable to the z slice thickness of the confocal microscope, the out-of-plane intensity contribution will be smaller, and the measurement will be less skewed. Hence, the two-component model works for smaller inclusions in predicting the anisotropy of the aggregated protein, but not for the large and bright inclusions. Nevertheless, it can be argued that because the large and bright inclusions have intensity values much higher (by 10−20-fold) than that of the diffusible protein present in the proximity, the fluorescence anisotropy value observed for a bright inclusion is more likely to be close to the actual fluorescence anisotropy of the aggregated protein present in the inclusion (Figure 4B).

Figure 6B shows the spread of the r_A values obtained by fitting the individual pixel-wise distributions of 25 faint inclusions (left panel) and 15 intermediate inclusions to eq 6 (middle panel). The r_A values obtained for the faint and intermediate inclusions were compared with the fluorescence anisotropy values observed in multiple bright inclusions. The data in Figure 6 show that the r_A values for the faint inclusions fall within a rather broad range (0.13−0.19) and are significantly higher than the measured fluorescence anisotropy values for bright inclusions, which are dispersed over a fairly narrow range (0.1−0.118). Because the value of r_A obtained from the model is likely to be a lower bound (see above), the actual value of aggregate anisotropy in faint inclusions would likely be significantly higher than that in bright inclusions. The observed and predicted r_A values for inclusions with intermediate intensity values are contained within the range of 0.12−0.16. Most of these values are higher than the anisotropy values observed for bright inclusions but lower than the observed anisotropy values of the majority of faint inclusions and the predicted anisotropy values of a few faint inclusions. Because the predicted value of r_A represents a lower bound on the actual value of aggregate anisotropy, the calculated r_A values suggest a gradual decrease in anisotropy because of gradual enhancement of homo-FRET, with an increase in the size and brightness of the inclusions.

TRA Decay Traces from Inclusions Display Multi-exponential Decay Components. TRA decay measurements were conducted for two reasons. (1) A change in anisotropy that can be attributed to homo-FRET will manifest itself as a fast component in the TRA decay. When present, this fast homo-FRET-allowed component will be independent of diffusible monomer concentration, which will not show homo-FRET. (2) The TRA measurements kinetically resolve the contribution of homo-FRET from that of rotational depolarization, as homo-FRET occurs over a much shorter time scale (within the first few nanoseconds of the decay), as compared to the much slower rotational depolarization (typically >10 ns for EGFP).[33,50] Thus, TRA decay measurements can reveal directly the mechanism by which emitted fluorescence is depolarized during the fluorescence lifetime of an excited fluorophore.

Figure 7 shows the TRA decays of diffusible and aggregated 74Q-mEGFP protein in cells. Each TRA measurement was made from a single point in a cell by accumulating the emitted photons for 30−60 s (see Materials and Methods). The TRA decay from a cell diffusely expressing the 74Q-mEGFP protein is very similar to that from an mEGFP-alone-expressing cell (Figure 7A) and is described well by a single-exponential decay, signifying the slow rotational tumbling of the molecules in the cytoplasm (see Materials and Methods). The slightly slower tumbling of 74Q-mEGFP compared to that of mEGFP is caused by the extra length of the poly-Q peptide (~100 amino acid residues) added to the mEGFP moiety. Figure 7B shows a representative TRA trace from a bright and large 74Q-mEGFP inclusion. It shows a significant loss of anisotropy within the first 2 ns of the decay, compared to the TRA trace of the diffusible protein in an

dx.doi.org/10.1021/bi500383h | *Biochemistry* 2014, 53, 3621−3636

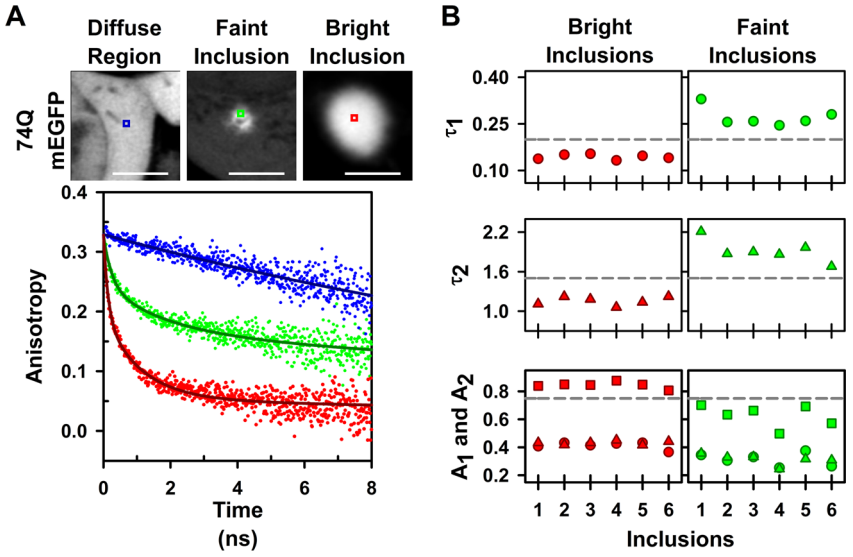

Figure 8. Time-resolved anisotropy decay measurements on faint and bright inclusions. (A) Intensity images of representative 74Q-mEGFP-expressing cells showing diffuse protein expression, a faint inclusion, and a bright inclusion. TRA traces were acquired from a single point, highlighted by the colored squares in the images. The plot shows the TRA traces representing the diffuse expression (blue circles), the faint inclusion (green circles), and the bright inclusion (red circles). The solid lines through the traces represent a single-exponential fit for the diffuse protein anisotropy decay trace, and three-exponential fits for the faint and bright inclusion anisotropy decay traces. (B) Time constants and amplitudes of the very fast (red and green circles) and fast (red and green triangles) decay components, along with their combined amplitudes (red and green squares) for six bright (red circles, triangles, and squares) and six faint (green circles, triangles, and squares) inclusions. The dashed gray lines have been drawn by inspection, only to facilitate the comparison. The intensity images have been rescaled to highlight the peak intensity of each individual image. The scale bar is 5 μm.

aggregate-free cell. This is typical for homo-FRET-dependent depolarization. The TRA trace appears to be relatively flat after the initial 2−3 ns of the decay, because the aggregated protein undergoes very slow rotational depolarization. The TRA decay curves from inclusions could not be described as single-exponential decays and were therefore analyzed as multi-exponential decays (Figure 7B). A two-exponential fit approximated the decay trace better than a single-exponential fit but also failed to fully describe the observed decay curve (Figure 7B). A three-exponential fit was found to describe the observed trace well and yields very fast and fast anisotropy decay times of ∼150 ps and 1.15 ns, respectively, for the TRA trace shown. The third component represents the slow tumbling of the aggregated protein and is slower than 40 ns. The very fast and fast decay components are also jointly responsible for >80% of the observed decay. This suggests that the majority of the mEGFP moieties in 74Q-mEGFP inclusions participate in homo-FRET. The very fast and fast decay components observed here are within the range (80 ps to 2.4 ns) of the homo-FRET-dependent TRA decay time constants observed previously in other GFP-based studies.[33,51]

Bright Inclusions Display a Higher Degree of Homo-FRET Than Fainter Inclusions. Figure 8 compares TRA decays from large and bright inclusions to those from relatively faint and small inclusions. The TRA decay trace from the fainter inclusion shows a considerable loss of anisotropy within the first 2 ns of decay, similar to the TRA decay trace from a bright inclusion (Figure 8A), but the extent of relative depolarization achieved in the first 2−3 ns is considerably smaller than that from a bright inclusion. This is highlighted by the high residual fluorescence anisotropy value at these time points of TRA decay of the faint inclusion compared to that of the bright inclusion (Figure 8A). The slope of the initial decrease in fluorescence anisotropy is also less steep in the TRA trace from the faint inclusion when compared to that from the bright inclusion. Figure 8B compares the very fast and fast anisotropy decay components, and their joint amplitudes, for multiple bright and faint inclusions. The observed very fast and fast anisotropy decay times are comparatively shorter for the bright inclusions. The combined amplitudes of the very fast and fast anisotropy decay times for bright inclusions also appear to be higher in comparison. This is indicative of a higher extent of homo-FRET in brighter inclusions.

DISCUSSION

In any given cell, an individual 74Q-mEGFP inclusion grows over time in both size and fluorescence intensity: it transforms from a small and faint inclusion into a large and bright inclusion (Figure S1 of the Supporting Information). However, because of the stochasticity of the aggregation process,[52] different cells commence inclusion formation at different times, so that at any given time point, different cells show inclusions that vary in size as well as in the intensity of the fluorescence of the mEGFP tag attached to the poly-Q tract. To study how the packing of aggregated protein within an inclusion changes with inclusion growth, either the growth of a smaller inclusion into a larger inclusion can be followed over time in a cell or inclusions of varying size and brightness present at the same time point in different cells can be directly compared by measurement of their SSA values. The latter strategy was followed in this study, because probing the same cell over a long time (∼5 h or more) taken for a small inclusion to become a larger one can cause photobleaching-induced variations in their SSA values.

It should be noted that the analysis of the SSA measurements on an inclusion yields a value for r_A that represents an average over the inclusion and does not take into account any heterogeneity in r_A values, in different regions of the inclusion. A comparison of such averaged r_A values across inclusions masks any differences in heterogeneity in the nature of internal packing with which different aggregates may be organized within an

dx.doi.org/10.1021/bi500383h | Biochemistry 2014, 53, 3621−3636

inclusion and between inclusions but is nevertheless useful in following how the average nature of packing changes as small and faint inclusions transform into large and bright inclusions. The averaged r_A value represents a lower bound on the average anisotropy value for all the aggregates distributed in a given inclusion, as shown in Figure 5.

It should also be noted that the individual inclusion-containing cells may also differ from each other because of heterogeneity in protein organization, for instance, because of the different inclusion morphology or assembly, and may not strictly represent the same inclusion growing with time (Figure 6A). For this particular reason, multiple inclusion-containing cells were first divided into broad classes of low-, intermediate-, and high-intensity values, and the average patterns of observed and fitted anisotropy (r_A) values were compared across classes (Figure 6B). Correlation of such average behavior with inclusion growth is justified as it would be highly unlikely that any of the analyzed 25 representative faint inclusions would not grow on to resemble any of the 25 bright inclusions in Figure 6B (as supported by the representative inclusion shown in Figure S1 of the Supporting Information).

Diffusely Expressed Protein Appears To Be Predominantly Monomeric. The SSA measurements from diffuse regions of 74Q-mEGFP-expressing cells yield high values of fluorescence anisotropy, similar to those obtained from non-pathogenic 23Q-mEGFP- and mEGFP-alone-expressing cells (Figure 1), suggesting that mainly monomeric protein is present in the aggregate-free regions of 74Q-mEGFP-expressing cells. TRA decay measurements were made from single confocal points in the diffuse-looking regions of cells, and the observation that the fluorescence anisotropy traces are described well as single-exponential decays, with a decay time of >20 ns, also suggests that monomeric protein is the dominant species in the diffusely expressing regions of cells. The presence of oligomers and small aggregates in these diffuse regions, however, cannot be ruled out as they may not be detected because of the strong dominance of highly populated monomeric protein.[53] The observed anisotropy in this case would be closer to that of the nonaggregated protein.

The Reduced Fluorescence Anisotropy Value of the mEGFP Moiety in the 74Q-mEGFP Inclusions Is Due to Extensive Homo-FRET. The utilization of mEGFP as the fluorescent tag on the poly-Q tract for measurement of the SSA has inherent advantages. mEGFP displays a rotational correlational time of >10 ns in solution (which will be longer in cells because of the higher cytoplasmic viscosity[54]), and an average fluorescence lifetime of ~2.5 ns. Because of the combined effects of a long anisotropy decay time and a relatively short fluorescence lifetime, mEGFP molecules retain a fairly high fluorescence anisotropy value.[33,48] More importantly, the contribution of rotational depolarization of the mEGFP moiety to the observed value of SSA is minimal.[55] Hence, any decrease in the fluorescence anisotropy of 74Q-mEGFP aggregates observed in this study can be attributed to homo-FRET between the mEGFP tags in the aggregates. This conclusion is supported by the observation that gradual photobleaching of the inclusions results in an increase in fluorescence anisotropy (Figure 3).

The SSA values observed in large and bright inclusions ($r \sim 0.11$) are substantially lower than those in aggregate-free diffuse regions ($r \sim 0.27$) of 74Q-mEGFP-expressing cells (Figure 2C). This observation that the fluorescence anisotropy of the 74Q-mEGFP aggregate within inclusions has decreased drastically in the large inclusions indicates that the distances separating the mEGFP moieties in the 74Q-mEGFP aggregate are comparable to the Förster radius of the mEGFP adduct, which is ~4.6 nm,[56] and that the mEGFP moieties are organized in the proximity of each other within relatively large clusters[30] within the inclusion. The value of aggregate anisotropy can be correlated directly with the extent of homo-FRET; the larger the extent of homo-FRET, the lower the anisotropy of an aggregate.

TRA Measurements Confirm the Occurrence of Homo-FRET and Reveal the Complexity of Aggregate Structure. When identical fluorophores are assembled in the proximity of each other, the occurrence of homo-FRET results in not only a decrease in SSA values but also the presence of initial fast depolarization in TRA decays. The observation of an initial fast depolarization, within the first 2−3 ns, in the TRA decay curves of 74Q-mEGFP inclusions (Figures 7B and 8A) is, therefore, a direct evidence of the occurrence of strong homo-FRET within the inclusions. In the large and bright inclusions, the fluorescence anisotropy value has decreased to less than one-third of the initial value ($r_0 \sim 0.32$) within the first 2 ns of the TRA decay, when homo-FRET is complete. Such a large change in fluorescence anisotropy has not been observed in other EGFP-based polarization studies,[33,43,50,57] suggesting that the 74Q-mEGFP molecules are very closely organized in large clusters. Although it may be possible to relate the cluster size with the extent of homo-FRET observed,[58] it is not so straightforward for mEGFP-labeled proteins,[57] but it would appear that the cluster size of 74Q-mEGFP molecules undergoing homo-FRET in large inclusions is at least greater than 3.[30]

Rather surprisingly, the homo-FRET component of the TRA decay curves cannot be described as a single-exponential decay. Instead, the homo-FRET-related anisotropy decay appears to occur with two rates. The very fast and fast TRA decay rates of the mEGFP moieties in the inclusions appear to be an outcome of the stoichiometry and geometry of fluorophore arrangements or simply a feature associated with large cluster sizes.[34,58,59] The two decay times are likely to represent at least two distinct FRET regimes, which may differ in either interfluorophore distances and/or relative fluorophore orientations or may simply point toward an underlying heterogeneity with which different aggregates may be packed within an inclusion. Currently, it is not possible to interpret the complex homo-FRET component of the decay quantitatively, but the apparent rates and amplitudes can be used to draw qualitative conclusions.

The homo-FRET-associated decay rates observed in bright inclusions are relatively faster than those observed in faint inclusions (Figure 8). The total amplitude of the homo-FRET component of the TRA decay that is over within 2−3 ns (Figure 8) is greater for the large inclusions than for the small inclusions. This result indicates that the cluster of 74Q-mEGFP molecules undergoing homo-FRET is greater in the large than in the small inclusions. It should be noted that the greater the number of molecules in a given cluster, the greater the overall probability of occurrence of homo-FRET. The TRA decay measurements suggest that a bright inclusion contains a greater concentration of aggregated 74Q-mEGFP molecules, and these molecules are more closely packed, when compared with a relatively faint inclusion. Because a faint inclusion represents an early precursor of a bright inclusion, it appears that the growth of an inclusion may be associated with a gradual increase in the packing density of the aggregating protein.

The Organization of Protein Molecules in 74Q-mEGFP Inclusions Changes Gradually with Growth. The extent of homo-FRET-allowed depolarization in the inclusions depends

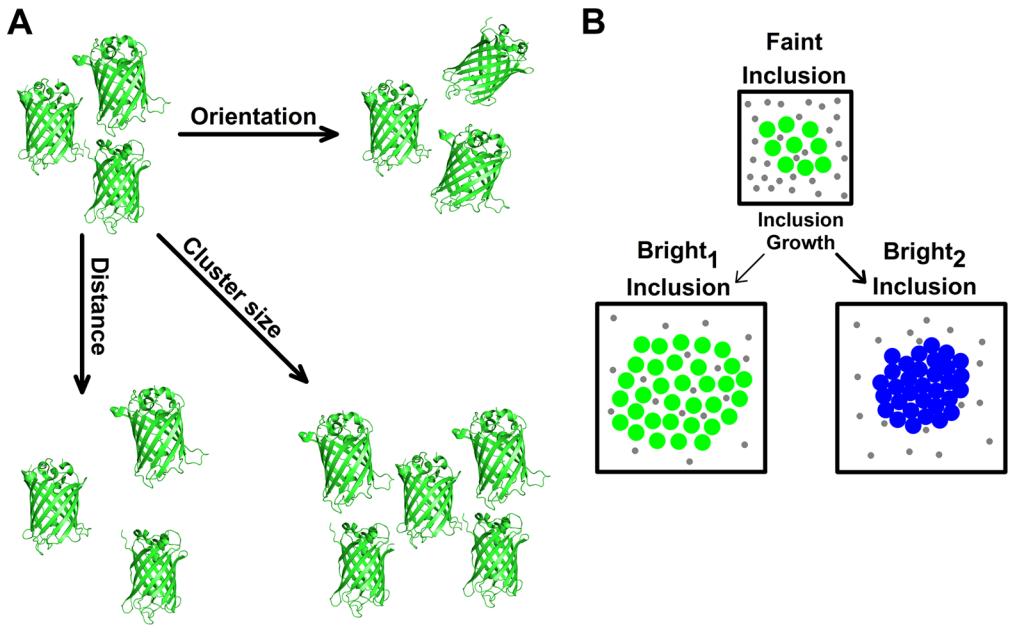

Figure 9. Origin of multiple homo-FRET components, models of inclusion growth, and arrangements of the aggregated protein in the 74Q-mEGFP inclusions. (A) Schematic of multiple mEGFP molecules organized with different interfluorophore distances, orientations, and clustering. (B) Schematic models of inclusion growth. The inclusion models shown contain diffusible protein (small gray circles, high anisotropy) and aggregates (large colored circles, low anisotropy). The faint inclusion and the bright$_1$ inclusion differ in the relative content of aggregated and diffusible protein, but the fluorescence anisotropy value of the aggregated protein is the same (green) in both cases. The bright inclusions shown differ in the way the aggregated protein is organized in them. The bright$_2$ inclusion has protein aggregates organized more closely, resulting in a reduced anisotropy of the aggregated protein (blue).

on the number of 74Q-mEGFP molecules in the proximity (the size of the cluster),[30] the distances separating the mEGFP adducts, and the relative orientations of the mEGFP adducts with respect to each other. The SSA measurements indicate that the extent of homo-FRET is enhanced as small and faint inclusions transform gradually into larger and brighter inclusions (see Results). The enhancement of homo-FRET in the large and bright inclusions as compared to the smaller and fainter inclusions is also supported by the observation that the rates of fast depolarization observed in the TRA measurements (Figure 8) are faster in the former than in the latter. Thus, the changes in anisotropy correlated with inclusion brightness, observed in this study, could result from changes in the 74Q-mEGFP packing density but could also arise from changes in the relative orientations of the mEGFP adducts. It is also possible that the enhancement of the homo-FRET rates may itself be a manifestation of increased cluster size,[34,58] which itself implies an increase in the level of protein packing, so that more fluorophores can undergo FRET with each other. In either case, the enhancement of homo-FRET would be caused by structural changes occurring within the inclusion as a small and faint inclusion grows into a larger and brighter inclusion.

The large change in the extent of depolarization observed as the small inclusions grow into large inclusions (see Results) makes it unlikely that the decrease in anisotropy can be accounted for by only a change in the relative fluorophore dipole orientation,[60] without a concomitant decrease in interfluorophore separation or an increase in cluster size. It is of course possible that in the large and bright inclusions, the mEGFP moieties, which are large barrel-shaped proteins (2.4 nm in width and 4.2 nm in length),[61] are clustered in the closest possible contact[33] in a set of specific nonrandom orientations that allow for high homo-FRET efficiency as well as extent of depolarization. It has been argued that the interactions between mEGFP barrels in the proximity can specify a set of specific nonrandom orientations.[57] The lower homo-FRET efficiency as well as the much lower level of depolarization seen in the smaller inclusions suggests that the set of specific nonrandom fluorophore orientations that are present in the large inclusions are different in the smaller inclusions. This is likely because the mEGFP moieties have not yet come into the closest possible contact specified by interactions between the mEGFP barrels. In other words, in this scenario, the mEGFP moieties would have to be more separated in the small inclusions than in the bright inclusions. Further, it is possible that just as the presence of the mEGFP tag may possibly affect the aggregation of 74Q-mEGFP (as described above), the presence of the rest of the structure in intact huntingtin protein would also modulate the aggregation process of the poly-Q tract that drives aggregation. These effects will have to be investigated in future studies.

Thus, while it is likely that changes in the relative orientations between the 74Q-mEGFP molecules may occur as the inclusion grows with addition of more 74Q-mEGFP protein, it is unlikely that these changes occur without a concomitant decrease in the distances separating the mEGFP adducts or an increase in the relative cluster size available for homo-FRET. Hence, it is likely that the structural changes in the aggregate that occur with inclusion growth (see above) are accompanied by an increase in packing density. Indeed, the observation that the intensity of an inclusion increases by nearly 10-fold (Figure S1 of the Supporting Information), a factor too large to be attributed to imperfect confocality (see above), as it grows from small to large, supports the possibility that inclusion growth is accompanied by an increase in packing density.

The Organization of mEGFP-Tagged Aggregated Protein Molecules in Inclusions and the Mode of Inclusion Growth. A simple model[21] of inclusion bodies in mammalian cells envisages them to be assemblies of aggregates.

dx.doi.org/10.1021/bi500383h | *Biochemistry* 2014, 53, 3621−3636

In the simplest of such cases, the inclusion may represent a region of higher aggregate concentration, without any interaggregate association [bright$_1$ inclusion (Figure 9)]. In this study, the homo-FRET measurements suggest the possibility that as small inclusions transform into large inclusions, changes in the packing of the 74Q-mEGFP molecules occur throughout the inclusion, including the center. The results are consistent with a model in which inclusion growth is accompanied by an increase in packing density. Speculatively, the growth of an inclusion may occur by integration of individual aggregate structures at the molecular level [bright$_2$ inclusion (Figure 9)], especially at the center of the inclusion. In such a possible scenario, an internal rearrangement of aggregate structure would have to occur after the association of the aggregates to form inclusions, and the larger the inclusion, the greater the internal structural rearrangement leading to a higher packing density at the inclusion center. It is possible that the increase in cluster size at the center of inclusions, which accompanies inclusion growth, may be a signature of such an internal structural rearrangement. It is also to be noted that if an inclusion were to form by simple juxtaposition of smaller aggregates, then it is possible that homo-FRET will increase and anisotropy will decrease, but only at the interaggregate interface present at the periphery of the inclusion. Accordingly, a decrease in anisotropy would not be observed at the center of the inclusion, contrary to the observation made in this study (Figures 2 and 6).

At the other extreme, inclusion growth might occur by addition of monomeric protein. If monomeric protein were to add only at the periphery of a growing inclusion, then this addition would have to be accompanied by internal packing rearrangement as described above for aggregate growth occurring by the assembly of smaller aggregates. Larger inclusions have been shown to have distinct cores,[62] and for such inclusions, recruitment of new protein has been shown to happen only at the periphery, which is less densely packed. It is possible, however, that monomeric protein can diffuse into the center and other parts of a small inclusion that is packed loosely, and its integration into the inclusion there leads to an increase in the level of homo-FRET and an increase in packing density. The stage at which the interior of an inclusion becomes sufficiently tightly packed for monomeric protein to be prevented from diffusing into it remains to be determined. In future studies, it would be interesting to study inclusion body formation as a crossover from diffusion-limited aggregation to a more compact growth.[63]

Biological Relevance of This Study. This study, utilizing fluorescence anisotropy as an elegant probe for examining structural variations between homo-oligomeric aggregates, has suggested that as inclusions grow inside cells, structural changes occur within them that affect internal packing and that packing density increases within the core. The TRA measurements have revealed heterogeneity in aggregate structures, which might explain the observation[27,62] that poly-Q aggregates have heterogeneous molecular interactions with associated proteins. It has been proposed that the presence of inclusion bodies may be toxic because they can sequester other proteins whose functions are important for cellular survival.[25,64] Indeed, large inclusion bodies have been shown to bind transcription factors but only at their periphery.[62] This study suggests that at early stages of inclusion body growth, before they become too densely packed, small inclusions may be more capable of sequestering functionally important protein or may interact with different sets of proteins compared to large inclusions. Indeed, it has been suggested that early inclusions, and not late and large inclusions, along with the diffusible protein may be the principal toxic forms.[17]

The homo-FRET-based assay described here for studying aggregate growth will be useful in designing high-throughput screening assays for testing the ability of different molecules to induce or prevent inclusion growth. It is known that protein aggregation is strongly affected by the conditions of aggregation, and this may possibly affect the underlying pathogenesis. For instance, aggregates formed by osmotic stress seem to differ from those induced by aging.[65] Homo-FRET-dependent analysis may represent an attractive way of comparing such structures, providing information at the level of molecular arrangement.

■ ASSOCIATED CONTENT

Ⓢ Supporting Information

Representative images of a cell, showing the growth of a poly-Q inclusion with time (Figure S1), and the method used for following inclusion growth. This material is available free of charge via the Internet at http://pubs.acs.org.

■ AUTHOR INFORMATION

Corresponding Author

*E-mail: jayant@ncbs.res.in. Telephone: 91-80-23666150. Fax: 91-80-23636662.

Funding

This work was funded by the Tata Institute of Fundamental Research and by the Department of Biotechnology, Government of India. J.B.U. is a recipient of a J. C. Bose National Research Fellowship from the Government of India.

Notes

The authors declare no competing financial interest.

■ ACKNOWLEDGMENTS

We thank David Rubinsztein for providing the two poly-Q EGFP constructs and Jyotsna Dhawan for help with cell lines. We thank M. K. Mathew, Madan Rao, Mukund Thattai, and G. Krishnamoorthy for discussions and for comments on the manuscript and Satyajit Mayor and his lab members for help with instrumentation and for discussions. Steady-state fluorescence anisotropy imaging and multiphoton excitation-based time-resolved fluorescence anisotropy decay trace acquisition were conducted at the Central Imaging Facility of the National Centre for Biological Sciences.

■ ABBREVIATIONS

mEGFP, monomeric enhanced green fluorescent protein; poly-Q, polyglutamine; FRET, Förster (fluorescence) resonance energy transfer; FRAP, fluorescence recovery after photobleaching; FLIP, fluorescence loss in photobleaching; SSA, steady-state anisotropy; TRA, time-resolved anisotropy; 74Q-mEGFP (poly-Q74) and 23Q-mEGFP (poly-Q23), mEGFP-tagged huntingtin exon 1 fragment with 74 and 23 glutamine residues, respectively; *I* and *r*, intensity and anisotropy, respectively; D and A, diffusible and aggregated protein, respectively; TCSPC, time-correlated single-photon counting.

■ REFERENCES

(1) Ross, C. A., Wood, J. D., Schilling, G., Peters, M. F., Nucifora, F. C., Cooper, J. K., Sharp, A. H., Margolis, R. L., and Borchelt, D. R. (1999) Polyglutamine pathogenesis. *Philos. Trans. R. Soc. London, Ser. B 354*, 1005−1011.

(2) Ross, C. A., and Poirier, M. A. (2004) Protein aggregation and neurodegenerative disease. *Nat. Med. 10* (Suppl.), S10−S17.
(3) Scherzinger, E., Lurz, R., Turmaine, M., Mangiarini, L., Hollenbach, B., Hasenbank, R., Bates, G. P., Davies, S. W., Lehrach, H., and Wanker, E. E. (1997) Huntingtin-encoded polyglutamine expansions form amyloid-like protein aggregates in vitro and in vivo. *Cell 90*, 549−558.
(4) DiFiglia, M., Sapp, E., Chase, K. O., Davies, S. W., Bates, G. P., Vonsattel, J. P., and Aronin, N. (1997) Aggregation of huntingtin in neuronal intranuclear inclusions and dystrophic neurites in brain. *Science 277*, 1990−1993.
(5) Finkbeiner, S. (2011) Huntington's Disease. *Cold Spring Harbor Perspect. Biol. 3* (6), a007476.
(6) Davies, S. W., Turmaine, M., Cozens, B. A., DiFiglia, M., Sharp, A. H., Ross, C. A., Scherzinger, E., Wanker, E. E., Mangiarini, L., and Bates, G. P. (1997) Formation of neuronal intranuclear inclusions underlies the neurological dysfunction in mice transgenic for the HD mutation. *Cell 90*, 537−548.
(7) Becher, M. W., Kotzuk, J. A., Sharp, A. H., Davies, S. W., Bates, G. P., Price, D. L., and Ross, C. A. (1998) Intranuclear neuronal inclusions in Huntington's disease and dentatorubral and pallidoluysian atrophy: Correlation between the density of inclusions and IT15 CAG triplet repeat length. *Neurobiol. Dis. 4*, 387−397.
(8) Li, S. H., and Li, X. J. (1998) Aggregation of N-terminal huntingtin is dependent on the length of its glutamine repeats. *Hum. Mol. Genet. 7*, 777−782.
(9) Scherzinger, E., Sittler, A., Schweiger, K., Heiser, V., Lurz, R., Hasenbank, R., Bates, G. P., Lehrach, H., and Wanker, E. E. (1999) Self-assembly of polyglutamine-containing huntingtin fragments into amyloid-like fibrils: Implications for Huntington's disease pathology. *Proc. Natl. Acad. Sci. U.S.A. 96*, 4604−4609.
(10) Poirier, M. A., Li, H., Macosko, J., Cai, S., Amzel, M., and Ross, C. A. (2002) Huntingtin spheroids and protofibrils as precursors in polyglutamine fibrilization. *J. Biol. Chem. 277*, 41032−41037.
(11) Thakur, A. K., Jayaraman, M., Mishra, R., Thakur, M., Chellgren, V. M., Byeon, I.-J. L., Anjum, D. H., Kodali, R., Creamer, T. P., Conway, J. F., Gronenborn, A. M., and Wetzel, R. (2009) Polyglutamine disruption of the huntingtin exon 1 N terminus triggers a complex aggregation mechanism. *Nat. Struct. Mol. Biol. 16*, 380−389.
(12) Legleiter, J., Mitchell, E., Lotz, G. P., Sapp, E., Ng, C., DiFiglia, M., Thompson, L. M., and Muchowski, P. J. (2010) Mutant huntingtin fragments form oligomers in a polyglutamine length-dependent manner in vitro and in vivo. *J. Biol. Chem. 285*, 14777−14790.
(13) Chen, S., Ferrone, F. A., and Wetzel, R. (2002) Huntington's disease age-of-onset linked to polyglutamine aggregation nucleation. *Proc. Natl. Acad. Sci. U.S.A. 99*, 11884−11889.
(14) Kar, K., Jayaraman, M., Sahoo, B., Kodali, R., and Wetzel, R. (2011) Critical nucleus size for disease-related polyglutamine aggregation is repeat-length dependent. *Nat. Struct. Mol. Biol. 18*, 328−336.
(15) Cooper, J. K., Schilling, G., Peters, M. F., Herring, W. J., Sharp, A. H., Kaminsky, Z., Masone, J., Khan, F. A., Delanoy, M., Borchelt, D. R., Dawson, V. L., Dawson, T. M., and Ross, C. A. (1998) Truncated N-terminal fragments of huntingtin with expanded glutamine repeats form nuclear and cytoplasmic aggregates in cell culture. *Hum. Mol. Genet. 7*, 783−790.
(16) Kaganovich, D., Kopito, R., and Frydman, J. (2008) Misfolded proteins partition between two distinct quality control compartments. *Nature 454*, 1088−1095.
(17) Arrasate, M., Mitra, S., Schweitzer, E. S., Segal, M. R., and Finkbeiner, S. (2004) Inclusion body formation reduces levels of mutant huntingtin and the risk of neuronal death. *Nature 431*, 805−810.
(18) Miller, J., Arrasate, M., Brooks, E., Libeu, C. P., Legleiter, J., Hatters, D., Curtis, J., Cheung, K., Krishnan, P., Mitra, S., Widjaja, K., Shaby, B. A., Lotz, G. P., Newhouse, Y., Mitchell, E. J., Osmand, A., Gray, M., Thulasiramin, V., Saudou, F., Segal, M., Yang, X. W., Masliah, E., Thompson, L. M., Muchowski, P. J., Weisgraber, K. H., and Finkbeiner, S. (2011) Identifying polyglutamine protein species in situ that best predict neurodegeneration. *Nat. Chem. Biol. 7*, 925−934.
(19) Takahashi, T., Kikuchi, S., Katada, S., Nagai, Y., Nishizawa, M., and Onodera, O. (2008) Soluble polyglutamine oligomers formed prior to inclusion body formation are cytotoxic. *Hum. Mol. Genet. 17*, 345−356.
(20) Lajoie, P., and Snapp, E. L. (2010) Formation and toxicity of soluble polyglutamine oligomers in living cells. *PLoS One 5*, e15245.
(21) Kopito, R. R. (2000) Aggresomes, inclusion bodies and protein aggregation. *Trends Cell Biol. 10*, 524−530.
(22) Muchowski, P. J., Ning, K., D'Souza-Schorey, C., and Fields, S. (2002) Requirement of an intact microtubule cytoskeleton for aggregation and inclusion body formation by a mutant huntingtin fragment. *Proc. Natl. Acad. Sci. U.S.A. 99*, 727−732.
(23) Waelter, S., Boeddrich, A., Lurz, R., Scherzinger, E., Lueder, G., Lehrach, H., and Wanker, E. E. (2001) Accumulation of mutant huntingtin fragments in aggresome-like inclusion bodies as a result of insufficient protein degradation. *Mol. Biol. Cell 12*, 1393−1407.
(24) Moulder, K. L., Onodera, O., Burke, J. R., Strittmatter, W. J., and Johnson, E. M. (1999) Generation of neuronal intranuclear inclusions by polyglutamine-GFP: Analysis of inclusion clearance and toxicity as a function of polyglutamine length. *J. Neurosci. 19*, 705−715.
(25) Chai, Y., Shao, J., Miller, V. M., Williams, A., and Paulson, H. L. (2002) Live-cell imaging reveals divergent intracellular dynamics of polyglutamine disease proteins and supports a sequestration model of pathogenesis. *Proc. Natl. Acad. Sci. U.S.A. 99*, 9310−9315.
(26) Rajan, R. S., Illing, M. E., Bence, N. F., and Kopito, R. R. (2001) Specificity in intracellular protein aggregation and inclusion body formation. *Proc. Natl. Acad. Sci. U.S.A. 98*, 13060−13065.
(27) Kim, S., Nollen, E. A. A., Kitagawa, K., Bindokas, V. P., and Morimoto, R. I. (2002) Polyglutamine protein aggregates are dynamic. *Nat. Cell Biol. 4*, 826−831.
(28) Narain, Y., Wyttenbach, A., Rankin, J., Furlong, R. A., and Rubinsztein, D. C. (1999) A molecular investigation of true dominance in Huntington's disease. *J. Med. Genet. 36*, 739−746.
(29) Weber, G. (1954) Dependence of the polarization of the fluorescence on the concentration. *Trans. Faraday Soc. 50*, 552−555.
(30) Runnels, L. W., and Scarlata, S. F. (1995) Theory and application of fluorescence homotransfer to melittin oligomerization. *Biophys. J. 69*, 1569−1583.
(31) Van Ham, T. J., Esposito, A., Kumita, J. R., Hsu, S. T. D., Kaminski Schierle, G. S., Kaminski, C. F., Dobson, C. M., Nollen, E. A. A., and Bertoncini, C. W. (2010) Towards multiparametric fluorescent imaging of amyloid formation: Studies of a YFP model of α-synuclein aggregation. *J. Mol. Biol. 395*, 627−642.
(32) Roberti, M. J., Jovin, T. M., and Jares-Erijman, E. (2011) Confocal fluorescence anisotropy and FRAP imaging of α-synuclein amyloid aggregates in living cells. *PLoS One 6*, e23338.
(33) Gautier, I., Tramier, M., Durieux, C., Coppey, J., Pansu, R. B., Nicolas, J. C., Kemnitz, K., and Coppey-Moisan, M. (2001) Homo-FRET microscopy in living cells to measure monomer-dimer transition of GFP-tagged proteins. *Biophys. J. 80*, 3000−3008.
(34) Nguyen, T. A., Sarkar, P., Veetil, J. V., Koushik, S. V., and Vogel, S. S. (2012) Fluorescence polarization and fluctuation analysis monitors subunit proximity, stoichiometry, and protein complex hydrodynamics. *PLoS One 7*, e38209.
(35) Ghukasyan, V., Hsu, C. C., Liu, C. R., Kao, F. J., and Cheng, T. H. (2010) Fluorescence lifetime dynamics of enhanced green fluorescent protein in protein aggregates with expanded polyglutamine. *J. Biomed. Opt. 15*, 016008.
(36) Varma, R., and Mayor, S. (1998) GPI-anchored proteins are organized in submicron domains at the cell surface. *Nature 394*, 798−801.
(37) Ganguly, S., Clayton, A. H. A., and Chattopadhyay, A. (2011) Organization of higher-order oligomers of the serotonin$_{1A}$ receptor explored utilizing homo-FRET in live cells. *Biophys. J. 100*, 361−368.
(38) Zacharias, D. A., Violin, J. D., Newton, A. C., and Tsien, R. Y. (2002) Partitioning of lipid-modified monomeric GFPs into membrane microdomains of live cells. *Science 296*, 913−916.
(39) Goswami, D., Gowrishankar, K., Bilgrami, S., Ghosh, S., Raghupathy, R., Chadda, R., Vishwakarma, R., Rao, M., and Mayor, S.

(2008) Nanoclusters of GPI-anchored proteins are formed by cortical actin-driven activity. *Cell 135*, 1085−1097.
(40) Snapp, E. L., Altan, N., Lippincott-Schwartz, J. (2003) Measuring protein mobility by photobleaching GFP chimeras in living cells. *Current Protocols in Cell Biology*, Chapter 21, Unit 21.1, Wiley, New York.
(41) Schindelin, J., Arganda-Carreras, I., Frise, E., Kaynig, V., Longair, M., Pietzsch, T., Preibisch, S., Rueden, C., Saalfeld, S., Schmid, B., Tinevez, J. Y., White, D. J., Hartenstein, V., Eliceiri, K., Tomancak, P., and Cardona, A. (2012) Fiji: An open-source platform for biological-image analysis. *Nat. Methods 9*, 676−682.
(42) Preibisch, S., Saalfeld, S., Schindelin, J., and Tomancak, P. (2010) Software for bead-based registration of selective plane illumination microscopy data. *Nat. Methods 7*, 418−419.
(43) Altman, D., Goswami, D., Hasson, T., Spudich, J. A., and Mayor, S. (2007) Precise positioning of myosin VI on endocytic vesicles in vivo. *PLoS Biol. 5*, e210.
(44) Mukai, H., Isagawa, T., Goyama, E., Tanaka, S., Bence, N. F., Tamura, A., Ono, Y., and Kopito, R. R. (2005) Formation of morphologically similar globular aggregates from diverse aggregation-prone proteins in mammalian cells. *Proc. Natl. Acad. Sci. U.S.A. 102*, 10887−10892.
(45) Fiumara, F., Fioriti, L., Kandel, E. R., and Hendrickson, W. A. (2010) Essential role of coiled coils for aggregation and activity of Q/N-rich prions and PolyQ proteins. *Cell 143*, 1121−1135.
(46) Olzscha, H., Schermann, S. M., Woerner, A. C., Pinkert, S., Hecht, M. H., Tartaglia, G. G., Vendruscolo, M., Hayer-Hartl, M., Hartl, F. U., and Vabulas, R. M. (2011) Amyloid-like aggregates sequester numerous metastable proteins with essential cellular functions. *Cell 144*, 67−78.
(47) Axelrod, D. (1979) Carbocyanine dye orientation in red cell membrane studied by microscopic fluorescence polarization. *Biophys. J. 26*, 557−573.
(48) Volkmer, A., Subramaniam, V., Birch, D. J., and Jovin, T. M. (2000) One- and two-photon excited fluorescence lifetimes and anisotropy decays of green fluorescent proteins. *Biophys. J. 78*, 1589−1598.
(49) Squire, A., Verveer, P. J., Rocks, O., and Bastiaens, P. I. H. (2004) Red-edge anisotropy microscopy enables dynamic imaging of homo-FRET between green fluorescent proteins in cells. *J. Struct. Biol. 147*, 62−69.
(50) Sharma, P., Varma, R., Sarasij, R. C., Ira, Gousset, K., Krishnamoorthy, G., Rao, M., and Mayor, S. (2004) Nanoscale organization of multiple GPI-anchored proteins in living cell membranes. *Cell 116*, 577−589.
(51) Vyas, N., Goswami, D., Manonmani, A., Sharma, P., Ranganath, H. A., VijayRaghavan, K., Shashidhara, L. S., Sowdhamini, R., and Mayor, S. (2008) Nanoscale organization of hedgehog is essential for long-range signaling. *Cell 133*, 1214−1227.
(52) Colby, D. W., Cassady, J. P., Lin, G. C., Ingram, V. M., and Wittrup, K. D. (2006) Stochastic kinetics of intracellular huntingtin aggregate formation. *Nat. Chem. Biol. 2*, 319−323.
(53) Ossato, G., Digman, M. A., Aiken, C., Lukacsovich, T., Marsh, J. L., and Gratton, E. (2010) A two-step path to inclusion formation of huntingtin peptides revealed by number and brightness analysis. *Biophys. J. 98*, 3078−3085.
(54) Swaminathan, R., Hoang, C. P., and Verkman, A. S. (1997) Photobleaching recovery and anisotropy decay of green fluorescent protein GFP-S65T in solution and cells: Cytoplasmic viscosity probed by green fluorescent protein translational and rotational diffusion. *Biophys. J. 72*, 1900−1907.
(55) Subramaniam, V., Hanley, Q. S., Clayton, A. H. A., and Jovin, T. M. (2003) Photophysics of green and red fluorescent proteins: Implications for quantitative microscopy. *Methods Enzymol. 360*, 178−201.
(56) Patterson, G. H., Piston, D. W., and Barisas, B. G. (2000) Förster distances between green fluorescent protein pairs. *Anal. Biochem. 284*, 438−440.
(57) Bader, A. N., Hofman, E. G., Voortman, J., en Henegouwen, P. M. P. V. B., and Gerritsen, H. C. (2009) Homo-FRET imaging enables quantification of protein cluster sizes with subcellular resolution. *Biophys. J. 97*, 2613−2622.
(58) Vogel, S. S., Thaler, C., Blank, P. S., and Koushik, S. V. (2009) Time Resolved Fluorescence Anisotropy. *FLIM Microsc. Biol. Med. 1*, 245−288.
(59) Marushchak, D., and Johansson, L. B. (2005) On the quantitative treatment of donor-donor energy migration in regularly aggregated proteins. *J. Fluoresc. 15*, 797−803.
(60) Mattheyses, A. L., Kampmann, M., Atkinson, C. E., and Simon, S. M. (2010) Fluorescence anisotropy reveals order and disorder of protein domains in the nuclear pore complex. *Biophys. J. 99*, 1706−1717.
(61) Ormö, M., Cubitt, A. B., Kallio, K., Gross, L. A., Tsien, R. Y., and Remington, S. J. (1996) Crystal structure of the *Aequorea victoria* green fluorescent protein. *Science 273*, 1392−1395.
(62) Matsumoto, G., Kim, S., and Morimoto, R. I. (2006) Huntingtin and mutant SOD1 form aggregate structures with distinct molecular properties in human cells. *J. Biol. Chem. 281*, 4477−4485.
(63) Georgalis, Y., Umbach, P., Raptis, J., and Saenger, W. (1997) Lysozyme aggregation studied by light scattering. I. Influence of concentration and nature of electrolytes. *Acta Crystallogr. D53*, 691−702.
(64) Preisinger, E., Jordan, B. M., Kazantsev, A., and Housman, D. (1999) Evidence for a recruitment and sequestration mechanism in Huntington's disease. *Philos. Trans. R. Soc. London, Ser. B 354*, 1029−1034.
(65) Moronetti Mazzeo, L. E., Dersh, D., Boccitto, M., Kalb, R. G., and Lamitina, T. (2012) Stress and aging induce distinct polyQ protein aggregation states. *Proc. Natl. Acad. Sci. U.S.A. 109*, 10587−10592.